Check for updates

Hydrogeochemical characteristics of thermal springs in the Qilian–Haiyuan fault zone at the northeast Tibetan Plateau: Role of fluids and seismic activity

Chenhua Li[1]*, Xiaocheng Zhou[2]*, Jingchao Li[2], Lei Liu[3],
Hejun Su[1], Ying Li[2]*, Miao He[2], Jinyuan Dong[2], Jiao Tian[2],
Huiling Zhou[1], Gang Gao[4], Caiyan Zhang[4] and Zhixin Luo[2]

[1]Gansu Lanzhou Geophysics National Observation and Research Station, Earthquake Administration of
Gansu Province, Lanzhou Institute of Geotechnique and Earthquake, CEA, Lanzhou, China, [2]Institute
of Earthquake Forecasting, China Earthquake Administration, Beijing, China, [3]Qinghai Earthquake
Agency, Xining, China, [4]Gansu Earthquake Agency, Lanzhou, China

The Qilian–Haiyuan fault zone (QHF) is located in a highly deformed and seismically active area of the northeastern margin of the Tibetan Plateau. This study investigated the major elements, strontium, hydrogen, and oxygen isotopes of 22 sites in the thermal springs along the QHF from October to November 2020. The QHF hydrochemical system is recharged by meteoric water primarily infiltrating between 2.8 and 4.4 km a.s.l. Based on quartz geothermometers, the geothermal reservoir temperature variation ranged from 25.5 to 111.3°C, and the circulation depth ranged from 1.3 to 5.6 km. In the QHF zone, the highest spring water temperature values were correlated with deep groundwater circulation circuits in areas where earthquake foci are concentrated. A conceptual model of the hydrologic cycle of thermal springs explains the spatial distribution of earthquakes associated with tectonic movements. The fluid circulation of the QHF corresponds well with the seismicity, which indicates that the hydrological characteristics of the thermal spring in a fault zone are vital in receiving information on seismic activity to assess the seismic risk of the QHF in the future.

KEYWORDS
hydrogeochemical characteristics, thermal springs, Qilian–Haiyuan fault zone, Tibetan Plateau, active seismicity

1 Highlights

- Fluid origin, reservoir temperature, and genesis of thermal waters along the Qilian–Haiyuan Fault (QHF) are constrained.
- Segmental hydrogeochemical characteristic of thermal springs in the QHF correlates well with the spatial distribution of seismic activities.

2 Introduction

The seismically active fault zones provide conduits for the upwelling of hydrothermal fluids in active tectonic settings (e.g., among many others, Arno et al., 2014; Chiodini et al., 2020). Meanwhile, geothermal fluid circulating along the fault increases increasing pore fluid pressure, triggering earthquakes and weakening the rock (e.g., among many others, Chiodini et al., 2011; Zuza and Cao, 2020). Over the years and all around the world, a large number of variations in hydrochemical parameters have been tentatively put in relation with the occurrence of earthquakes (e.g., among many others, Barberio et al., 2017; Claesson et al., 2004; Onda et al., 2018; Reddy et al., 2017; Schuessler et al., 2016; Li et al., 2021; Gori and Barberio, 2022). Previous studies have revealed that the circulation depth, reservoir temperature, and geochemistry of hydrothermal fluids are affected by fault structures involved in earthquake nucleation over variable spatial scales, including microscale fractures in dilated rocks of individual faults and kilometer-scale fault displacements across the lithosphere (e.g., among many others, Scott et al., 2020). This provides a physicochemical basis for exploring the possible relationships between fluid geochemistry and seismic activities along the active faults.

According to the official measurement of the China Seismic Network, the Ms 6.9 earthquake with a 10-km focal depth occurred in Menyuan County, Haibei Prefecture, Qinghai (37.77°N, 101.26°E) at 01:45 on 8 January 2022 (Beijing time). The earthquake resulted in a surface rupture of about 22 km due to the sinistral strike-slip motions. The Lanxin high-speed railway, passing through the fault, suffered severe damage. The earthquake occurred in the western Qilian–Haiyuan fault zone (QHF), the Lenglongling fault segment, which has been very active for many large earthquakes in history (Li et al., 2022). This could facilitate acquiring the geochemical information about the deep fluid associated with earthquakes to perform hydrological and geochemical monitoring of regions with intense seismic activities. However, previous studies have focused on the source of heat and chemical characteristics of some springs in this area. Few studies have examined the relationship between the hydrochemical characteristics of hot springs and fault activity. Such studies are essential for evaluating the geothermal energy potential along the fracture zone. This study focuses on the hydrochemical properties and origin of 22 thermal springs in the QHF. Major and trace elements, $^{87}Sr/^{86}Sr$ values, δD, and $\delta^{18}O$ values were discussed to characterize these hot springs' hydrochemical properties. The quartz geothermometers were employed to calculate their reservoir temperature and water circulation depth to reveal their possible hydrochemical evolution processes. We aimed to discuss the relationship between hot spring evolution and seismic activity through a conceptual model

of the hot spring hydrology cycle, combined with the temporal variation characteristics of the chemical composition of one thermal spring continuously monitored since May 2020, prospecting its implications for future monitoring.

3 Geological and seismotectonic setting

The QHF is located on the northeastern margin of the Qinghai–Tibet Plateau. The Qilian Mountains are subjected to the continuous uplift and northeastward compressive deformation of the Tibetan Plateau (Zhang et al., 2003; Zhang et al., 2006; Lei et al., 2020), forming a series of northwest-southwest strip-like mountains controlled by late Quaternary thrust faults, strike-slip faults, and active folds, about 700 km long (Yuan et al., 2004; Yuan et al., 2013). The Qilian Shan–Hexi corridor can be regarded as a compressional zone of two strike-slip faults—the Altun Fault and Haiyuan Fault—where crustal shortening and mountain uplift caused by many thrusts and folds in the region coordinated the transition and balance between the two faults (Yuan et al., 2004; Zhang et al., 2017). Faults that developed in the region from the west to the east include the Altun Fault, Jinta South Mountain Fault, Yumu Mountain Fault, North Rim Fault of Qilian Mountains, Changma–Ebo Fault, Tuole Mountain Fault, Lenglongling Fault, and Maomao Mountain–Lahu Mountain–Haiyuan Fault (Figure 1A,B). The crustal deformation in this area is intense, and seismic activity is frequent. Since the 20th century, this area has experienced several earthquakes, such as the Ms 8.5 Haiyuan earthquake in 1920, the Ms 8.0 Gulang earthquake in 1927, the Ms 7.6 Changma earthquake in 1932, the Ms 7.25 Shandan earthquake in 1954, and the Ms 7 Gonghe earthquake in 1990 (Supplementary Table S1). The epicenter of the Ms 6.9 Menyuan earthquake is located in the western segment of the Lenglongling fault zone in the middle and western segments of the generalized Haiyuan fault. The fault is a Holocene active fault with a sinistral strike-slip nature and a fault slip rate of about 4–8 mm/a. The eastern end of the fault is connected with the Gulang and Maomaoshan faults, and the western end is connected with the Tuolaishan Fault, with a total length of 130 km (Yang et al., 2022).

The thermal springs selected in this study are mainly distributed in the Northern Rim Fault of the Qilian Mountains, the Altun Fault, Yumu Mountain Fault, Lenglongling Fault, and Maomao Mountain Fault–Laohu Mountain Fault–Haiyuan Fault zone (Figure 1). The Qilian Mountains is about 1000 km long from east to west and is the birthplace of groundwater and surface water in the Hexi region (Geng, et al., 2017). The annual average precipitation and evaporation values are 298.9 and 3038.1 mm, respectively, and
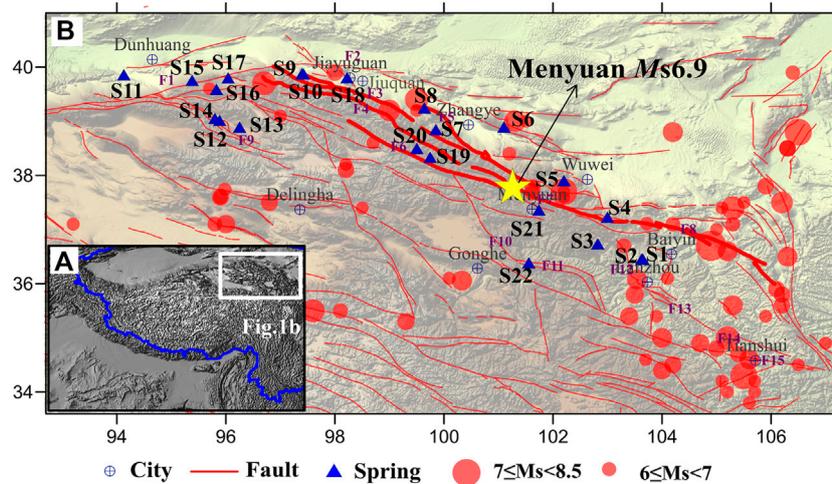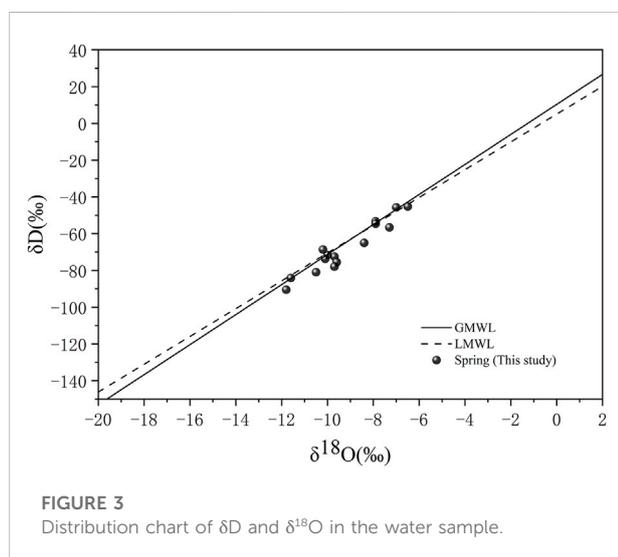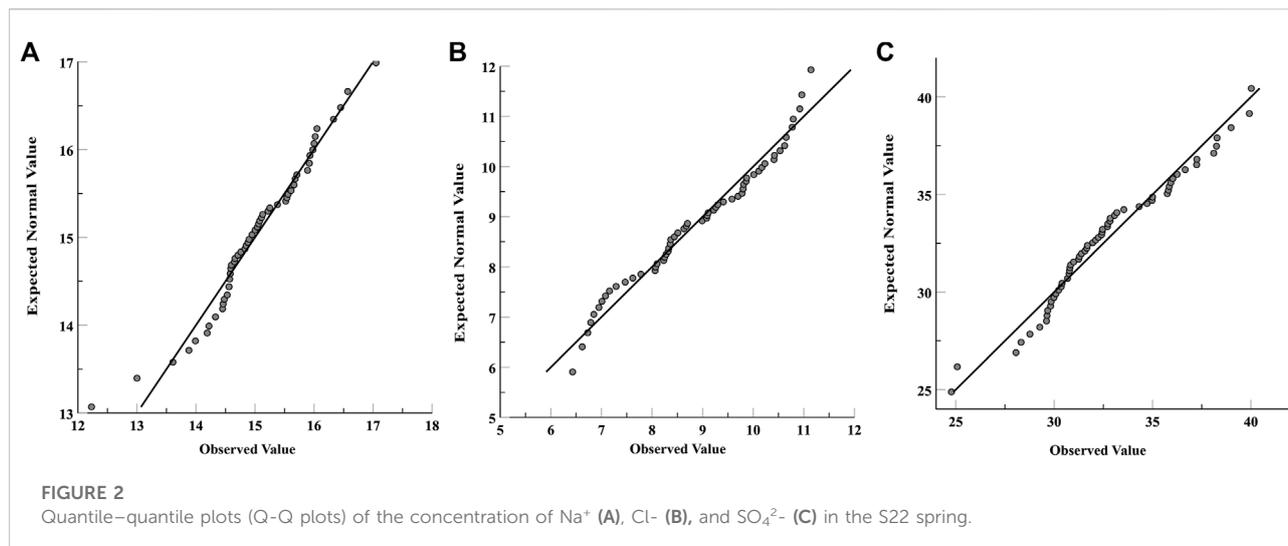
FIGURE 1
(A) Macro-regional map; **(B)** location of water sampling points and foci of large earthquakes (Ms >6), along with major fault traces (F1: Altun Fault; F2: Jinta South Mountain Fault; North Edge Fault of Qilian Mountain; F4: Changma-Ebo Fault; F5: Yumu Mountain Fault; F6: Tuole Mountain Fault; F7: Lenglongling Fault; F8: Haiyuan Fault; F9: Danghe South Mountain Fault; F10: Riyue Mountain Fault; F11: Laji Mountain Fault; F12: Zhuanglang River Fault; F13: Majie Mountain Fault; F14: Tongwei Fault; F15: Fault of north edge of West Qinling. The time of $Ms \geq 6$ earthquake is from BC780 to 12 January 2022 (Supplementary Table S1). The blue line in Figure 1a represents the borderline. The seismicity data came from the National Earthquake Data Center of China https://data.earthquake.cn/datashare/report.shtml?PAGEID=earthquake_zhengshi).

the annual temperature ranges from −3.0 to 4.0°C. Many rivers originating from the high-altitude areas of the Qilian Mountains incise the tectonically active margin, generating strikingly steep topography and mobilizing large volumes of sediment before flowing into the arid Hexi corridor, including the Heihe River, the Shule River, and the Shiyang River (Meng et al., 2020). Rivers originating in the Qilian Mountains are the primary recharge source for groundwater in the study area. The mountain aquifers are mainly fractured, weathered rocks and in deep structural fractured zones, with direct hydraulic interaction. Water circulates fast through the fractures. Thus, groundwater is commonly connected with the surface water and is directly recharged from snow-melt and glacial ice melt (Zhao et al., 2018).

4 Material and methods

Groundwater samples were collected from 22 thermal springs along the QHF in October 2020 (Figure 1B and Supplementary Table S2). Supplementary Table S3 shows the geochemical analysis of water sampled every 3 days taken from the spring S22 since May 2021. All water samples were collected in new, colorless, polyethylene terephthalate (PET) bottles that had been rinsed with the water samples. Then, the water samples were filtered through a 0.45-μm membrane. Samples were collected in five colorless polyethylene terephthalate (PET) bottles (50 ml) for major and trace

element concentrations, hydrogen and oxygen isotopes, and SiO_2 concentration analysis. Additionally, the samples were acidified with ultrapure HNO_3 for cation analysis but not acidified for anion analyses. Finally, the water samples were stored in a 4°C refrigerator, with laboratory analyses conducted within 2 weeks. The specific conductance, pH, dissolved oxygen, and temperature were measured in samples using a multiparameter probe inserted into a flow-through cell closed to the atmosphere and in springs by lowering the probe into the spring vent for *in situ* measurements. The concentrations of cations (K^+, Na^+, Mg^{2+}, and Ca^{2+}) and anions (F^-, Cl^-, Br^-, NO_3^-, and SO_4^{2-}) were measured using a Dionex ICS-900 ion chromatography system and an AS40 automatic sampler at the Earthquake Forecasting Key Lab of China Earthquake Administration, with ±2% reproducibility and 0.01 mg/L detection limits (Chen et al., 2015). The HCO_3^- and CO_3^{2-} concentrations in the thermal springs were measured by 0.05 mol/L HCl titration of 0.1% methyl orange and 1% phenolphthalein in procedures with a ZDJ-100 potentiometric titrator (within ±2% reproducibility). An inductively coupled plasma emission spectrometer Optima−5300 DV (PerkinElmer Inc.) was used to detect SiO_2. The hydrogen and oxygen isotopes were measured using a Finnigan MAT253 mass spectrometer, *via* the TC/EA method. Results were expressed as parts per thousand deviations from Vienna Standard Mean Ocean Water (V−SMOW). Precisions of ±0.2% (2 S.D.) and ±1%

FIGURE 2
Quantile−quantile plots (Q-Q plots) of the concentration of Na$^+$ **(A)**, Cl- **(B)**, and SO$_4^{2-}$ **(C)** in the S22 spring.

FIGURE 3
Distribution chart of δD and δ^{18}O in the water sample.

(2 S.D.) were obtained for δ^{18}O and δD in a standard water sample, respectively (Wang et al., 2010). Sr element and its isotope were analyzed at the Test Center of the Research Institute of Uranium Geology by Element XR ICP−MS (Thermo Fisher, Bremen, Germany) (Zhang et al., 2018). The data on the water chemicals were evaluated by calculating the ion balance (ib) (Baird et al., 2017). The threshold value of continuous monitoring was calculated according to the equation X+ σ and X+ 2σ (X: average value; σ: once of the standard deviation; 2σ: twice of the standard deviation, Supplementary Table S4). Additionally, since mean and standard deviation are estimated over an expected Gaussian distribution, the Gaussianity of the continuous monitoring value has been verified by the Q–Q (quantile–quantile) plots (Figure 2).

5 Results

5.1 Origin of the thermal spring water

The respective distribution ranges of the measured values of δD and δ^{18}O in the thermal spring water in the QHF are −90.4~−45.2‰ and −11.8~−6.5‰. In comparison with the global meteoric water line (δD = 8.17δ^{18}O + 10.35) (Rozanski et al., 1993) and the meteoric water line in the northwest region of China [δD = 7.56δ^{18}O + 5.05 (R^2 = 0.97)] (Huang et al., 2008), it could be observed that δD and δ^{18}O of the thermal spring water are mainly distributed near the meteoric water line (Figure 3), indicating that meteoric waters are the main recharge sources of the thermal spring. According to the relationship between δ^{18}O/ δD and recharge elevation (δ^{18}O = −0.00347ALT + 3.04; δD = −0.02585ALT + 28.28) (Wu et al., 2020), it could be calculated that the recharge elevation is about 2.8–4.4 km (Table 1), which is close to the elevation of nearby Qilian Mountains.

5.2 Origin of water-soluble ions in thermal springs

5.2.1 Origin of the major elements

In the thermal spring water of the QHF, the main positive ions include Ca^{2+}, Mg^{2+}, and Na$^+$, and the main negative ions are SO$_4^{2-}$ and HCO$_3^-$. The concentrations of various ions are significantly divided, and the water quality is complicated (Figure 4). In the piper chart, the water samples are mainly distributed in three areas. The water of the thermal spring points on the first zone of the piper diamond graph (S3, S4, S7, S12, S16, S21, and S22) belongs to the HCO$_3$−Ca·Mg type, especially distributed in the central area of the fault. The water

TABLE 1 Recharge elevation in the QHF.

No.	δ18O	δD	Recharge elevation (km)		
	(‰)		δ18O = −0.00347ALT + 3.04	δD = −0.02585ALT + 28.28	Mean
1	−10.5	−80.9	3.9	4.2	4.1
4	−7.9	−53.3	3.2	3.2	3.2
5	−9.7	−72.5	3.7	3.9	3.8
6	−10.0	−71.6	3.8	3.9	3.8
9	−10.1	−73.7	3.8	3.9	3.9
10	−9.6	−75.5	3.6	4.0	3.8
12	−9.7	−77.9	3.7	4.1	3.9
14	−11.8	−90.4	4.3	4.6	4.4
15	−11.6	−84.0	4.2	4.3	4.3
16	−8.4	−65.0	3.3	3.6	3.5
18	−7.9	−54.6	3.2	3.2	3.2
19	−7.0	−45.7	2.9	2.9	2.9
20	−6.5	−45.2	2.7	2.8	2.8
21	−7.3	−56.6	3.0	3.3	3.1
22	−10.2	−68.6	3.8	3.7	3.8

FIGURE 4
Piper trilinear nomograph for the water sample.
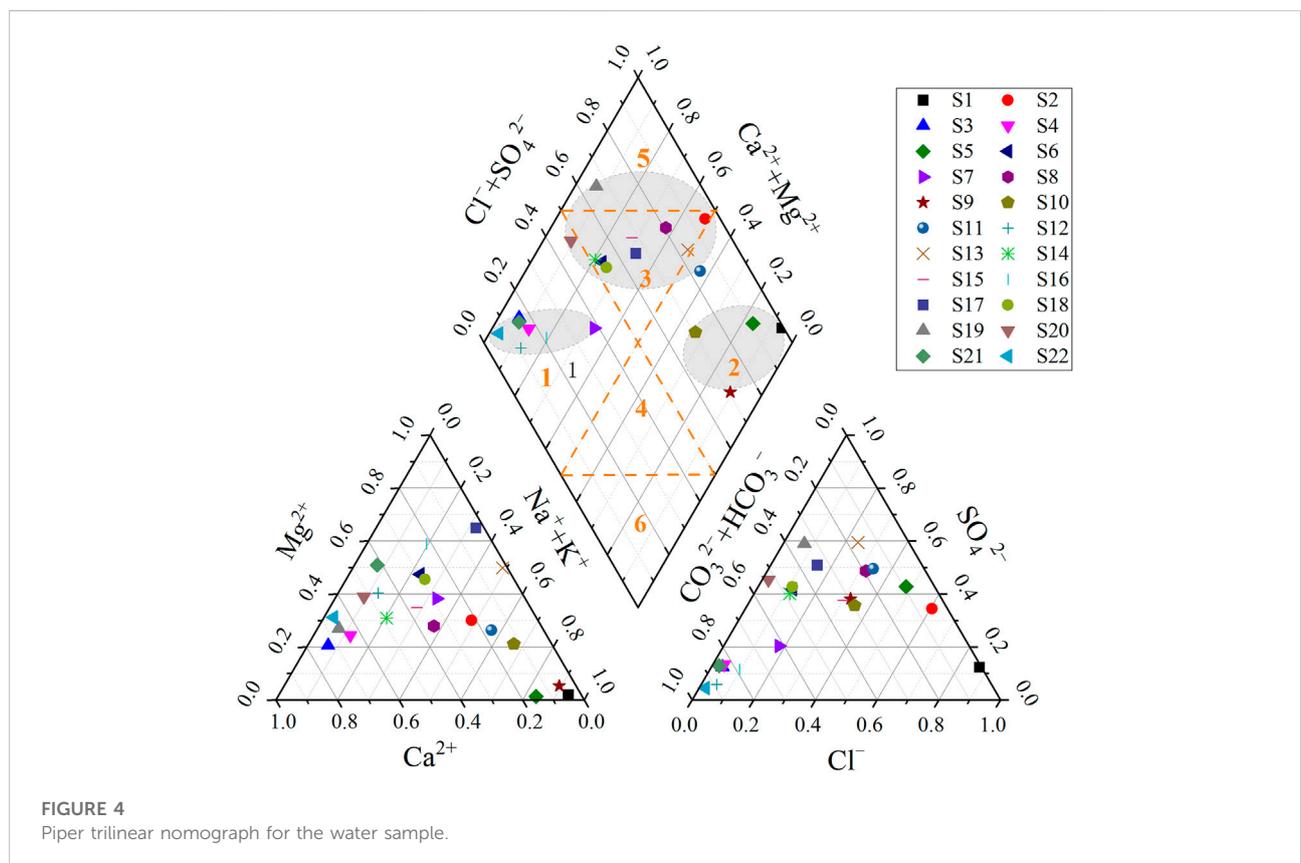
is mainly recharged by meteoric waters or meltwater from snow and ice from the Qilian Mountains. Geothermal water wells (deep groundwater; S1, S5, S9, and S10) in the second zone of the diamond graph, whose water belongs to the SO_4 (Cl)–Na type, mainly scatter on the northern segment piedmont fault of the Qilian Mountains, indicating that the meteoric waters or meltwater from snow and ice suffers the influence of evaporation and mutual interaction between water and rocks when passing through the basin of the Hexi corridor. Consequently, the mass concentrations of the main ions in the water are relatively high, consistent with the groundwater characteristics in the arid region of northwest China. Most other thermal spring water points are located in the third zone of the piper diamond graph. Such water belongs to the Ca–SO_4 type and scatters in the transition area between HCO_3–Ca·Mg type water and SO_4 (Cl)–Na type water (Figure 4). The results agree with previous studies, suggesting that the bedrock fissure water in the mountainous region was the belt for HCO_3–type water, the alluvial plains were the belt for the SO_4–type, and the desert and salinization areas are the belt for Cl–type water through the variation of the chemical characteristics of groundwater in the whole basin (Liu et al., 2004).

The constant elements in the thermal spring water of the Qilian Mountain Fault are closely related to the surrounding rocks, hydrodynamic force, and hydrothermal conditions. The Paleozoic strata in the research area are mainly constituted by plagioclase granite and sand–mudstone developed in the Cambrian period, fragmented rocks of monzonitic granite, and lime rocks developed in the Ordovician period, gabbro developed in the Silurian period, and diorite developed in the Devonian period and Carboniferous period. The Mesozoic strata mainly consist of quartz diorite developed in the Triassic period and Jurassic periods and granite developed in the Cretaceous period. The Precambrian strata scattered in some areas are primarily constituted by terrain developed in the Changcheng period. The rocks in the Pleistocene and Quaternary periods are mostly river flooding and windborne deposits (Su et al., 2016). Thus, the lithology of the body of the Qilian Mountain mainly comprises metamorphic rocks, tuff, sandstone, and dolomite, all of which are rich in calcium and magnesium. In the early formative period of the groundwater in the mountain, the surface water dissolved and filtered these rocks, leading to the saturation of calcite and dolomite. Consequently, the thermal spring water exposed to the central fault of the Qilian Mountain is mainly HCO_3–type water; the thermal spring water developed at the northern segment piedmont fault of the Qilian Mountain gradually transits into SO_4–type water due to the evaporation and filtering functions in the drought area; the deep circulation water within the basin of the Hexi corridor is mainly Cl–type water.
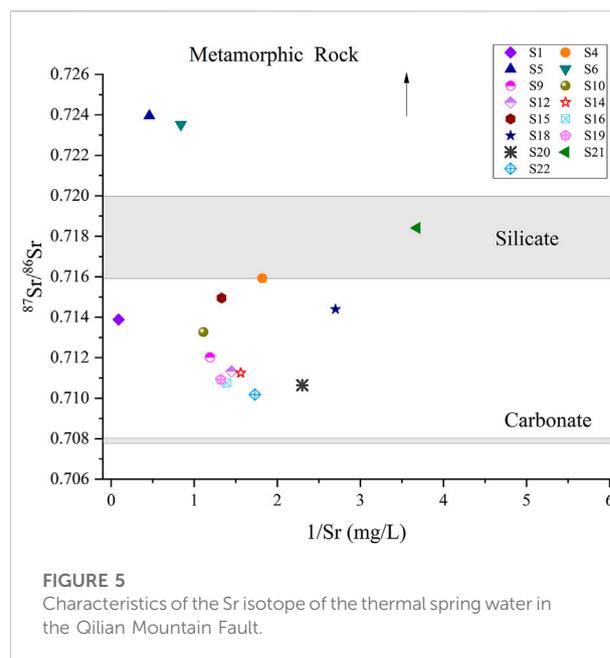

FIGURE 5
Characteristics of the Sr isotope of the thermal spring water in the Qilian Mountain Fault.

5.2.2 Sr isotope

The specific value of $^{87}Sr/^{86}Sr$ in the thermal spring is generally similar to that in the rock-forming minerals in contact with the water (e.g., Négrel et al., 1997; Capo et al., 1998; Millot et al., 2011). The constitution of the strontium isotope in spring water could reflect the lithologic characteristics of the pass-through stratum. Minerals like silicate, sulfate, and carbonate are the main sources of Sr element in the underground water, which significantly influence the specific value of $^{87}Sr/^{86}Sr$ in the underground water (Palmer and Edmond, 1992). Among them, the specific value of $^{87}Sr/^{86}Sr$ originating from weathering of sulfate and carbonate is about 0.708, whereas that originating from the weathering of aluminosilicate is generally from 0.716 to 0.720. The weathering product of metamorphic rocks has a higher specific value of $^{87}Sr/^{86}Sr$ (Wang et al., 2009; Tian et al., 2019). The value of $^{87}Sr/^{86}Sr$ in this study ranged from 0.710642 to 0.723948. Sr in the QHF mainly originates from the mixture of weathering products of silicate and carbonate rocks and weathering products of metamorphic rocks (S5, S6) (Figure 5). The value of $^{87}Sr/^{86}Sr$ of the thermal spring water in Guankou Town (S21) is 0.718415. Although it is the weathering product of silicate rock-type minerals, its chemical type is HCO_3–Mg (Ca). Therefore, it could be deduced that the water develops from the thermal spring water containing carbonate minerals after passing through the fault and silicate rocks. The water in Niuquangou (S4) had a similar situation. Previous studies believed that the metamorphic hydrothermal system formed from the landform uplift and fractures in the region of the Qilian Mountain has a high Sr isotope feature similar to that of the Himalayan region (Liu et al., 2022).
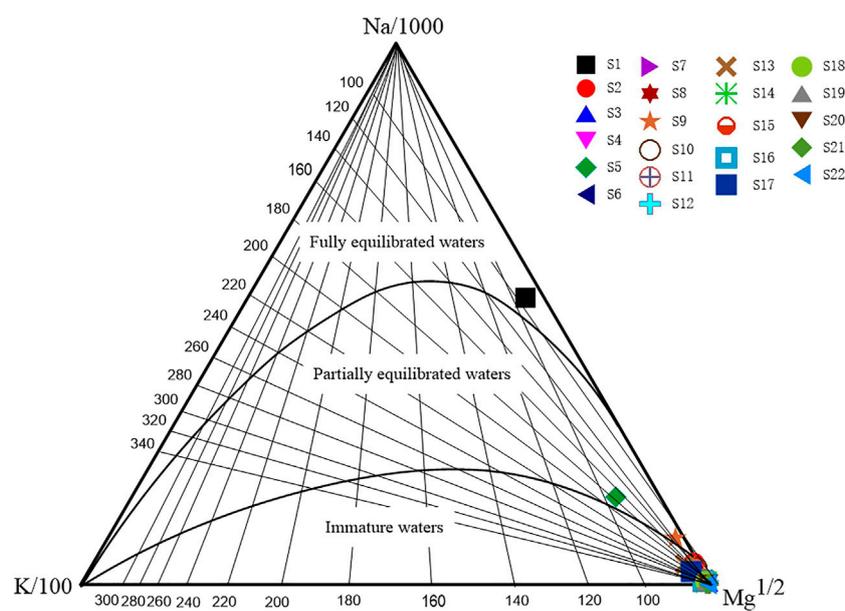
FIGURE 6
Na–K–Mg ternary diagram of the thermal spring water sample.

Moreover, the pH value of the thermal spring water in the fault zone of the Qilian Mountain ranged from 7.22 to 8.93, with a mean value of 7.85. Previous studies indicated that weak alkaline water with a pH value from 7.0 to 8.5 could easily enrich Sr^{2+} (Wang et al., 2009). The concentration of Sr^{2+} in the zone is 0.27 mg/L –11.50 mg/L, with a mean value of 1.56 mg/L, especially thermal spring S1 (NaCl-type water) has a significantly high concentration of Sr^{2+}.

5.3 Water–rock interaction of thermal springs when circulating inside the fault

Chemical equilibration was tested with a ternary diagram established using relative Na/1000, K/100, and $Mg^{1/2}$ contents (Giggenbach, 1988). The Na–K–Mg triangular plot (Figure 6) shows the S1 sample plot in the fully equilibrated water zone and S5 and S9 sample plots in the partial equilibrated water zone, located at the front rim of the fault on the north rim of the Qilian Mountain. Other thermal spring samples almost belong to immature waters, indicating that they are not fully equilibrated with the reservoir rocks.

Many chemical geothermometers are used to estimate reservoir temperatures (Fournier and Truesdel, 1973; Fournier and Potter, 1979; Fouillac and Michard, 1981; Fournier and Potter, 1982; Arnórsson, 1983; Chiodini et al., 1995). Various chemical geothermometers always yield very different reservoir temperatures because of the complex geological settings. The

generally used geothermometers include a cation and SiO_2 geothermometers. The cation geothermometers were suitable to estimate the reservoir temperature of the water–rock reaction equilibrium status, although most of the thermal spring water samples did not reach the water–rock equilibrium in this study, as indicated in Figure 6 (Fouillac and Michard, 1981; Fournier and Potter, 1982; Arnórsson, 1983; Chiodini et al., 1995). Therefore, we chose the quartz geothermometers with no steam loss and calculated the circulation depth (Table 2). Li et al. (2021) gave a detailed calculation method. The results showed that the reservoir temperature of the spring samples in the QHF ranged from 25.5 to 111.3°C.

According to the reservoir temperature, the circulated depth calculation formula shown as follows is adopted

$$Z = Z_0 + (T - T_0)/T_{grad}. \qquad (1)$$

Here, Z represents the circulation depth (km); Z_0 represents the depth of the constant temperature zone (km); T represents the reservoir temperature (°C); T_0 represents the temperature of the constant temperature zone (°C), namely, the local average temperature; T_{grad} represents the geothermal gradient (°C/km) reflecting the geothermal change per kilometer of the place below the constant temperature zone (Xiong et al., 1990). Based on the previous studies on groundwater in the Qilian Mountain, we selected the geothermal gradient T_{grad} of 20 C/km, the annual mean temperature T_0 in the Qilian Mountain is 0.37°C, and the

TABLE 2 Calculation of reservoir temperature and circulation depth.

No.	Temperature (°C)	SiO$_2$ (mg/L)	Reservoir temperature (°C)	Circulation depth (km)	Temperature difference between the spring vent and reservoir (°C)
S1	33.7	18.87	61.3	3.1	27.6
S4	6.4	7.37	29.7	1.5	23.3
S5	57.4	60.92	111.3	5.6	53.9
S6	16.3	15.40	53.9	2.7	37.6
S9	25.1	13.44	49.1	2.5	24.0
S10	13.8	11.16	42.9	2.2	29.1
S12	5.3	9.48	37.5	1.9	32.2
S14	5.9	8.33	33.4	1.7	27.5
S15	5.1	6.86	27.5	1.4	22.4
S16	3.7	20.02	63.5	3.2	59.8
S18	11.4	10.12	39.6	2.0	28.2
S19	3.7	6.41	25.5	1.3	21.8
S20	5.4	10.76	41.6	2.1	36.2
S21	7.0	6.58	26.3	1.3	19.3
S22	38.5	19.49	62.5	3.1	24.0

Z_0 is 30 m (Liu et al., 2020; Wu et al., 2020). The circulation depth along the QHF is about 1.3–5.6 km. The reservoir temperature of the thermal springs is positively associated with the circulation depth. The temperature difference between the spring vent and the reservoir indicated more mixing opportunities and a proportion of cool water during the longer groundwater circulation path (Table 2). The circulation depth of the thermal spring water in the S5 spring at the front basin of the Qilian Mountain Fault is the deepest, about 5.6 km deep, and the temperature difference is as high as 53.9°C. In contrast, the circulation depth of the thermal spring at the inter-mountain and front thrusting faults of the Qilian Mountain is shallower, about 1.5 km.
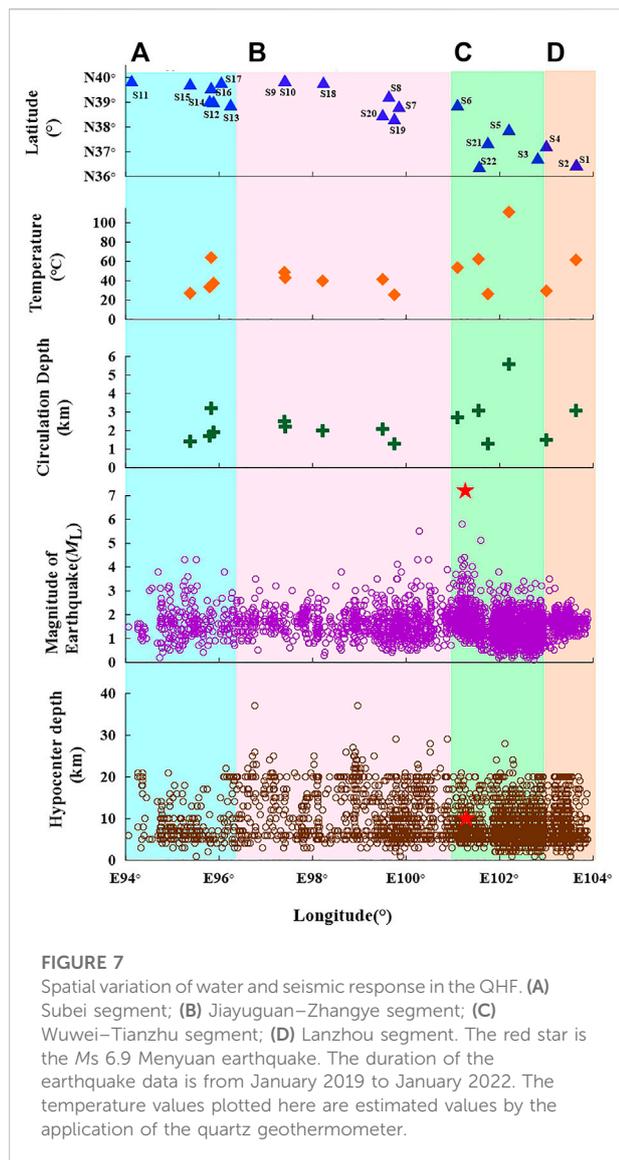
6 Discussion

6.1 The hydrological and geochemical spatial and temporal variation characteristics of the thermal spring and response to earthquakes

6.1.1 Spatial distribution characteristics of the thermal spring and earthquakes

The QHF is located in a transitional zone between the NE-striking Altyn Tagh Fault and E-striking Haiyuan Fault in the northeastern margin of the Tibetan Plateau (Meng et al., 2020), which is a focal zone with high earthquake risk. In this study, the 22 thermal springs were distributed along the four segments of

the QHF, namely, the Subei segment (a), Jiayuguan–Zhangye segment (b), Wuwei–Tianzhu segment (c), and Lanzhou segment (d). The ranking of the QHF spring waters in terms of thermal reservoir temperature, circulation depth, water maturity, and water–rock interaction intensity is roughly segmented c > segment a > segment d > segment b. The historical earthquakes in the QHF used to appear and gather in segment c (Figure 7). The estimated average reservoir temperature of the thermal springs displays a southeastward increasing trend along the QHF, with an obvious high geothermal zone focusing on the Wuwei–Tianzhu segment (c). In this segment, the highest spring water temperature values are correlated with deep groundwater circulation circuits in areas where the earthquake foci are concentrated (Figure 7). Generally, the geothermal fluids potentially influence the tectonic activities of this boundary fault. Previous studies have proposed that the reactivation of faults and migration of deep fluids in the fault system may be critical controlling factors for the regional seismic activity and geothermal anomalies (Doglioni et al., 2014; Wang et al., 2018).

Deep fluid circulation and facture coupling are important triggers of earthquakes. The pore fluid overpressure in active fault systems can drive fluid flow, causing fault weakening and seismicity. Snell et al. (2020) believed that non-linear, complex feedback between fluid flow, fluid pressure, and fault deformation controls the length of an earthquake's nucleation phase and the interseismic duration period in natural faults. Zuza and Cao (2020) suggested that geothermal gradients using high-resolution earthquake-location data from California to construct

FIGURE 7
Spatial variation of water and seismic response in the QHF. **(A)** Subei segment; **(B)** Jiayuguan–Zhangye segment; **(C)** Wuwei–Tianzhu segment; **(D)** Lanzhou segment. The red star is the *M*s 6.9 Menyuan earthquake. The duration of the earthquake data is from January 2019 to January 2022. The temperature values plotted here are estimated values by the application of the quartz geothermometer.

with the localized geothermal anomalies, suggesting potential genetic links between lithospheric thermal structure and earthquake nucleation along an active fault, similar to previous research in the southeastern and eastern Tibetan Plateau (Wang et al., 2018; Liu et al., 2022) and western North America (Wong and Chapman, 1990).

6.1.2 Temporal variation characteristics of thermal springs and response to the earthquake

The major ion concentrations of the Huangzhong Spring (S22) close to the epicenter, continuously monitored every 3 days since May 2021, did not display any obvious anomaly before the *M*s 6.9 Menyuan earthquake (Figure 8). The absence of the anomaly might be associated with a weak correlation in stress change because the spring is not on the same structural system as the earthquake's fault. The spring is located on the Laji Mountain Fault, while the earthquake is on the Lenglongling Fault (Figure 1). However, the concentrations of SO_4^{2-} and Cl^- fluctuated abnormally in the period from January 9 to 22 after the *M*s 6.9 Menyuan earthquake (Figure 8). Previous studies showed that the increase in the ion concentration indicated that stress accumulation promoted the development of pores within the fault zone, increasing the water–rock reaction surface (Zoback and Bverlee, 1975; Brace, 1978; Teufel, 1980; Sobolev, 1984; Claesson et al., 2007; Reddy et al., 2011; Woith et al., 2013; Chen et al., 2014; Rosen et al., 2018). Thus, we infer that the reason of no-anomaly detection at the geochemical monitoring site may be that the pre-earthquake strain accumulation in the Lenglongling Fault was not effectively transferred to adjacent faults. However, co-earthquake and post-earthquake strain release in the Lenglongling Fault was effectively transferred to the adjacent Laji Fault, which may be the cause of the post-earthquake anomaly.

Precursory changes occur in an area due to changes in the regional stress field associated with the onset of the earthquake process and the spatial pattern of these changes being non-uniform (Hauksson and Goddard, 1981; Wakita et al., 1985; Thomas et al., 1986; Utkin and Yurkov, 2010). Chen and Wang (2021) reported the major ion concentration changes in the Ganze Spring in response to the 2014 Ms 6.1 Yingjiang earthquake. Although the distance between the Ganze Spring and the epicenter was 320 km away, the spring is located in the tensile direction of the epicenter. However, no obvious hydrochemical responses in the Ganze Spring were observed during other earthquakes, which occurred within 100 km away from the Ganze Spring during the study period. For example, the 24 June 2012 *M*s 5.7 Ninglang earthquake and the 3 March 2013 *M*s 5.5 Eryuan earthquake indicated that earthquakes occurred in different directions of the regional stress even though they were close to the Ganze Spring. In the 1995 Kobe earthquake, for two wells within a distance of 50 m and of the same depth, one indicated changes in hydrochemistry associated with the earthquake, whereas the other did not (Wakita, 1996). These examples are related to the tectonic position of wells and the
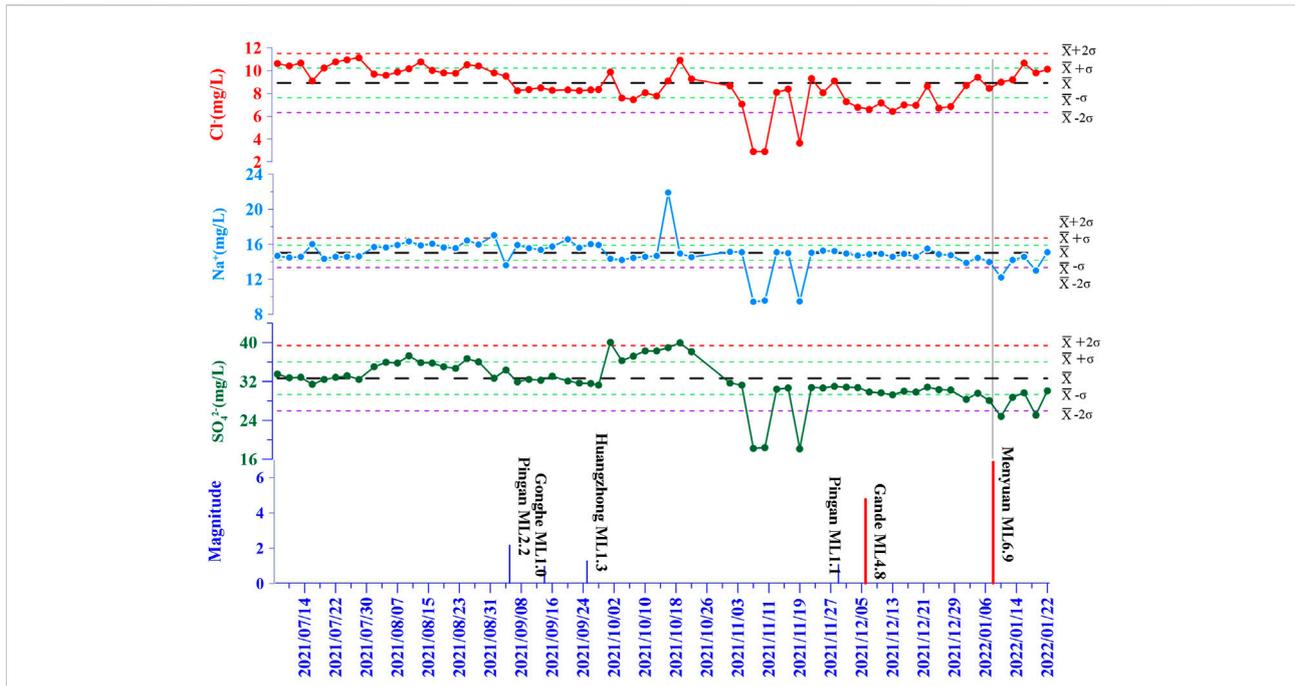
a topographic map of the base of the seismogenic crust mostly control the brittle-ductile transition depth. The activity of the geothermal fluid segment in the QHF is consistent with the more frequently occurring earthquake zone, which can be inferred that the distribution of geothermal anomalies in the QHF indicates localized seismic activity (Okada et al., 2015).

Moreover, most earthquakes along the QHF have focal depths ranging from 5 to 20 km, with the focal zone generally below the circulation depths of the thermal waters (1.3–5.6 km; Figure 7) but corresponding to the uppermost part of low-velocity and high-conductivity layers (Lei and Zhao, 2016). As shown in Figure 7, a comparison among fluid circulation depths and temperatures, numbers, and focal depths of earthquakes along the QHF suggests that earthquakes tend to occur beneath the regions with larger fluid circulation depths. This is consistent

FIGURE 8
Temporal variation of water and seismic response in the S22 spring (the blue vertical line indicates the earthquakes above *M*s 1.0 within the scope of 50 km, the red vertical line indicates the earthquakes above *M*s 4.0 within the scope from 50 to 300 km. The duration of data monitoring is from 30 May 2021 to 22 January 2022)
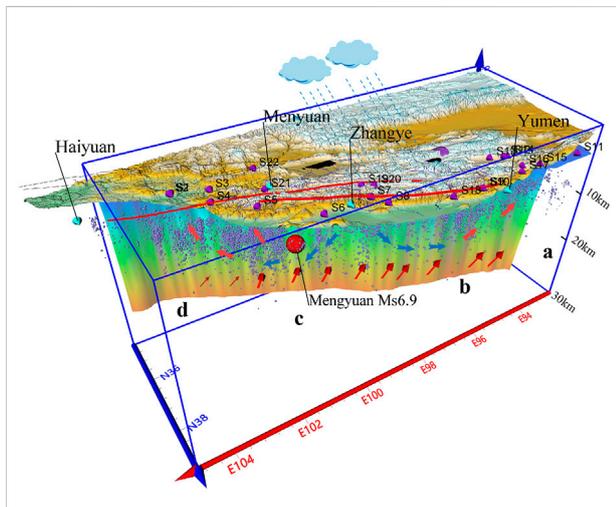

FIGURE 9
Conceptual model for the cause of formation of underground water and the hydrological geochemical circulation process.

seismic events is not only related to the magnitude and distance from the epicenter but is also controlled by the tectonic stress of deep major faults. To further address the spring responses to earthquakes, continuous monitoring of more hydrochemical parameters is suggested in the future, as already performed elsewhere (Pierotti et al., 2015, 2017; Gherardi and Pierotti, 2018).

6.2 The hydrogeochemical circulation model of thermal spring waters in the Qilianshan Fault

A conceptual model for the origin of the groundwater and the hydrogeochemical cycling process in the QHF was established based on previous geophysical data and this study's results (Figure 9). In the recharge area with an altitude of about 2.88–4.4 km, the meteoric waters in the Qilian mountainous area permeated into the aquifers along m4.4 km; the meteoric waters in the Qilian mountainous area permeated into the aquifers along mountain fractures and river terraces and then passed through the water–conducted zone to conduct deep circulation. When the circulation depth increases to 1.3–5.60 km and the reservoir condition reaches 25.5–111.3°C, the water would come across the water–rock reaction with rocks at different depths (like granite and igneous rock) under certain temperature and pressure conditions. Differences in the water–rock reaction degree result in partially

direction of the regional stress field associated with the onset of the earthquake process. This phenomenon may be universal and similar to this study. Considering the tectonic location and distance from the epicenter, it can be inferred that the response of hot springs to

balanced and immature water formation. When rising to the earth's surface, such water would be mixed with shallow cool water, finally becoming exposed on the earth's surface as a thermal spring. When the crustal stress in the QHF changes, the pressure in the aquifer system and the equilibrated state of thermal spring water would be disrupted, resulting in different hydro-chemical characteristics (Claesson et al., 2007; Kima et al., 2019). Therefore, continuous monitoring could be conducted on a proper hot spring spot of the fault zone to further study the pre-seismic hydrochemical precursors.

The results of this study indicate that faults are crucial in controlling the migration of crustal fluids. These maps can improve our knowledge of earthquake hazard models including potential rupture areas for fault zones and testing existing fault-hazard models against earthquake distributions. Meanwhile, more case studies are required to understand the entire system globally.

7 Conclusion

The detailed mechanism and process of geochemical characteristic changes in the QHF were described in terms of regional groundwater flow systems by using the hydrochemical data on the 22 thermal springs. The results suggested that the surrounding thermal spring water was mainly supplied from meteoric waters of the nearby mountains with a recharge elevation of about 2.8–4.4 km. The water chemical type is primarily controlled by the lithologic features of the aquifer. The thermal spring exposed at the central fault of the Qilian Mountain is mainly the HCO_3 type, while the thermal spring water developed at the front fault of the northern rim of the Qilian Mountain gradually became SO_4 type due to evaporation and filtering functions in the drought area. Moreover, the deep circulation water within the basin of the Hexi Corridor is mainly Cl type. The $^{86}Sr/^{87}Sr$ value indicated that the thermal spring containing carbonate minerals passed through the fault and flowed through the silicate rock before exposing it from the earth's surface.

The reservoir temperature of the thermal spring in the QHF was 25.5–111.3°C, and the circulation depth was 1.3–5.6 km. The circulation depth of the thermal spring water in the S5 spring at the front basin of the QHF is the deepest, which was about 5.6 km, and the temperature difference was as high as 53.9°C. Moreover, the water–rock reaction was in a partially equilibrated state. In contrast, the circulation depth of the thermal spring at the inter-mountain and front thrusting faults of the QHF is relatively shallow, about 1.5 km. Due to the weaker water–rock reaction, most of the spring is immature water.

The circulation depth at the fault of the mountainous areas of the Qilian Mountain is shallow due to the relatively strong stress

accumulation at the inter-mountain and front thrusting faults of the Qilian Mountain. The shallow fissure development results in a short water circulation path, leading to a weak water–rock reaction. However, for geothermal water in the basin on the mountain's front, the meteoric waters would pass leaching and deposits' evaporation on the basin, going through the more equilibrated water–rock reaction due to the longer circulation path.

The segmental characteristics of the fault, the hydration characteristics of the thermal springs located in different segments of the QHF, and the seismic activities are closely related. In particular, the springs in the Wuwei–Tianzhu segment had deeper recharge source and high reservoir temperatures than others. This coincided with strong tectonic and seismological activities in the Wuwei–Tianzhu segment. Thus, the spatial distribution of hot springs, the hydro-geochemical characteristics, and the influence of controlling factors are essential to further exploration of strong seismic information.

Data availability statement

The original contributions presented in the study are included in the article/Supplementary Material; further inquiries can be directed to the corresponding authors.

Author contributions

Conceptualization, CL and XZ; methodology, CL, XZ, and YL; software, JD; validation, JT; formal analysis, CL, MH, JT, and HS; investigation, CL, JL, HZ, GG, CZ, LL, and ZL; data curation, CL and XZ; writing—original draft preparation, JL; writing—review and editing, CL and XZ; visualization, CL; supervision, XZ, YL, and CL. All authors have read and agreed to the published version of the manuscript.

Funding

Acknowledgments

Conflict of interest

The authors declare that the research was conducted in the absence of any commercial or financial relationships that could be construed as a potential conflict of interest.

Publisher's note

Supplementary material

The Supplementary Material for this article can be found online at: https://www.frontiersin.org/articles/10.3389/feart.2022.927314/full#supplementary-material

References

Arno, Z., Volker, O., Philippe, J., Nicholas, D., Roland, G., Art, M., et al. (2014). Analysis of induced seismicity in geothermal reservoirs - an overview. *Geothermics* 52, 6–21. doi:10.1016/j.geothermics.2014.06.005

Arnórsson, S. (1983). Chemical equilibria in Icelandic geothermal systems-Implications for chemical geothermometry investigations. *Geothermics* 12, 119–128. doi:10.1016/0375-6505(83)90022-6

Baird, R. B., Eaton, A. D., and Rice, E. W. (2017). *Standard methods for examination of water and wastewater*. 23rd ed. Camden, NJ, USAWashington, DC, USA: American Public Health Association; American Water Works Association; Water Environment Federation.

Barberio, M. D., Barbieri, M., Billi, A., Doglioni, C., and Petitta, M. (2017). Hydrogeochemicalchanges before and during the 2016 Amatrice-Norcia seismic sequence (central Italy). *Sci. Rep.* 7 (1), 11735. doi:10.1038/s41598-017-11990-8

Brace, W. F. (1978). A note on permeability changes in geologic material due to stress. *PAGEOPH* 116, 627–633. doi:10.1007/bf00876529

Capo, R. C., Stewart, B. W., and Chadwick, O. A. (1998). Strontium isotopes as tracers of ecosystem processes: Theory and methods. *Geoderma* 82, 197–225. doi:10.1016/s0016-7061(97)00102-x

Chen, L., and Wang, G. C. (2021). Hydrochemical changes of a spring due to the May 30, 2014 Ms 6.1Yingjiang earthquake, southwest China. *Environ. Pollut.* 284, 117125–125. doi:10.1016/j.envpol.2021.117125

Chen, Z., Du, J., Zhou, X., Yi, L., Liu, L., Xie, C., et al. (2014). Hydrochemistry of the hot springs in western sichuan Province related to the WenchuanMS8.0 earthquake. *Sci. World J.* 2014, 901432. doi:10.1155/2014/901432

Chen, Z., Zhou, X., Du, J., Xie, C., Liu, L., Li, Y., et al. (2015). Hydrochemical characteristics of hot spring waters in the Kangding district related to the Lushan $M_S = 7.0$ earthquake in Sichuan, China. *Nat. Hazards Earth Syst. Sci.* 15, 1149–1156. doi:10.5194/nhess-15-1149-2015

Chiodini, G., Caliro, S., Cardellini, C., Frondini, F., Inguaggiato, S., and Matteucci, F. (2011). Geochemical evidence for and characterization of CO2 rich gas sources in the epicentral area of the Abruzzo 2009 earthquakes. *Earth Planet. Sci. Lett.* 304, 389–398. doi:10.1016/j.epsl.2011.02.016

Chiodini, G., Cardellini, C., Di Luccio, F., Selva, J., Frondini, F., Caliro, S., et al. (2020). Correlation between tectonic CO2 Earth degassing and seismicity is revealed by a 10-year record in the Apennines, Italy. *Sci. Adv.* 6, eabc2938. doi:10.1126/sciadv.abc2938

Chiodini, G., Frondini, F., and Marini, L. (1995). Theoretical geothermometers andPCO2 indicators for aqueous solutions coming from hydrothermal systems of medium-low temperature hosted in carbonate-evaporite rocks. Application to the thermal springs of the Etruscan Swell, Italy. *Appl. Geochem.* 10, 337–346. doi:10.1016/0883-2927(95)00006-6

Claesson, L., Skelton, A., Graham, C., Dietl, C., Morth, M., Torssander, P., et al. (2004). Hydrogeochemical changes before and after a major earthquake. *Geol.* 32 (8), 641. doi:10.1130/g20542.1

Claesson, L., Skelton, A., Graham, C., and Morth, C. M. (2007). The timescale and mechanisms of fault sealing and water-rock interaction after an earthquake. *Geofluids* 7 (4), 427–440. doi:10.1111/j.1468-8123.2007.00197.x

Doglioni, C., Barba, S., Carminati, E., and Riguzzi, F. (2014). Fault on–off versus coseismic fluids reaction. *Geosci. Front.* 5 (6), 767–780. doi:10.1016/j.gsf.2013.08.004

Fouillac, C., and Michard, G. (1981). Sodium/lithium ratio in water applied to geothermometry of geothermal reservoirs. *Geothermics* 10, 55–70. doi:10.1016/0375-6505(81)90025-0

Fournier, R. O., and Potter, R. W. (1982). A revised and expanded silica (quartz) geothermometer. *Geoth. Res. Counc. Bull.* 11, 3–9.

Fournier, R. O., and Potter, R. W. (1979). Magnesium correction to the Na-K-Ca chemical geothermometer. *Geochim. Cosmochim. Acta* 43, 1543–1550. doi:10.1016/0016-7037(79)90147-9

Fournier, R. O., and Truesdel, A. H. (1973). Empirical Na-K-Ca geothermometer for natural waters. *Geochim. Cosmochim. Acta* 37, 1255–1275.

Geng, H., Pan, B., Huang, B., Cao, B., and Gao, H. (2017). The spatial distribution of precipitation and topography in the Qilian Shan Mountains, northeastern Tibetan Plateau. *Geomorphology* 297, 43–54. doi:10.1016/j.geomorph.2017.08.050

Gherardi, F., and Pierotti, L. (2018). The suitability of the Pieve Fosciana hydrothermal system (Italy) as a detection site for geochemical seismic precursors. *Appl. Geochem.* 92, 166–179. doi:10.1016/j.apgeochem.2018.03.009

Giggenbach, W. F. (1988). Geothermal solute equilibria: Derivationof Na-K-Ma-Ca geoindicators. *Geochim. Cosmochim. Acta* 52, 2749–2765. doi:10.1016/0016-7037(88)90143-3

Gori, F., and Barberio, M. D. (2022). Hydrogeochemical changes before and during the 2019 Benevento seismic swarm in central-southern Italy. *J. Hydrol. X.* 604, 127250. doi:10.1016/j.jhydrol.2021.127250

Hauksson, E., and Goddard, J. (1981). Radon content of groundwater as an earthquake precursor: Evaluation of worldwide data and physical basis. *J. Geophys. Res.* 86, 9397–9410. doi:10.1029/jb086ib10p09397

Huang, T., Nie, Z. H., and Yuan, L. (2008). Temperature and geographical effects of hydrogen and oxygen isotopes in precipitation in west of China. *J. arid land Resour. Environ.* 22 (8), 76–81. (In Chinese).

Kima, J., Leea, J., Petitta, M., Kim, H., Kaown, D., Park, I. W., et al. (2019). Groundwater system responses to the 2016 ML 5.8 Gyeongju earthquake, South Korea. *J. Hydrology* 576, 150–163. doi:10.1016/j.jhydrol.2019.06.044

Lei, J., Li, Y., Oskin, M. E., Wang, Y., Xiong, J., Xin, W., et al. (2020). Segmented thrust faulting: Example from the northeastern margin of the Tibetan Plateau. *J. Geophys. Res. Solid Earth* 125, e2019JB018634. doi:10.1029/2019JB018634

Lei, J., and Zhao, D. (2016). Teleseismic P-wave tomography and mantle dynamics beneath Eastern Tibet. *Geochem. Geophys. Geosyst.* 17 (5), 1861–1884. doi:10.1002/2016GC006262

Li, C. H., Zhou, X. C., Yan, Y. C., Ouyang, S., and Liu, F. (2021). Hydrogeochemical characteristics of hot springs and their short-term seismic precursor anomalies along the xiaojiang fault zone, southeast Tibet Plateau. *Water* 13, 2638. doi:10.3390/w13192638

Li, Z., Gai, H., Li, X., Yuan, D., Xie, H., Jiang, W., et al. (2022). Seismogenic fault and coseismic surface deformation of the Menyuan Ms6.9 earthquake in Qinghai,

China. *Acta Geol. Sin.* 96 (1), 330–335. (In Chinese). doi:10.19762/j.cnki.dizhixuebao.2022124

Liu, F., Cao, G., Cao, S., and Yang, Y. (2020). Research on stable isotope characteristics and recharge relationship of the main river on the southern slope of Qilian Mountains. *J. desert Res.* 40 (6), 151–161. doi:10.7522/j.issn.1000-694X.2020.00085

Liu, W., Wang, T., Gao, X., and Su, Y. (2004). Distribution and evolution of water chemical characteristics in Heihe river basin. *J. desert Res.* 24 (6), 755–762. (In Chinese).

Liu, Y., Yang, Y., Song, B., Galy, A., Zhang, F., Jin, Z., et al. (2022). Hydrothermal systems with radiogenic Sr in the North Qaidam ultrahigh-pressure metamorphic belt, NE Tibetan Plateau and implications for regional dissolved Sr budget. *Appl. Geochem.* 138, 105214. doi:10.1016/j.apgeochem.2022.105214

Meng, K., Wang, E., Chu, J. J., Su, Z., and Fan, C. (2020). Late Cenozoic river system reorganization and its origin within the Qilian Shan, NE Tibet. *J. Struct. Geol.* 138, 104128. doi:10.1016/j.jsg.2020.104128

Millot, R., Guerrot, C., Innocent, C., Negrel, P., and Sanjuan, B. (2011). Chemical, multi-isotopic (Li–B–Sr–U–H–O) and thermal characterization of Triassic formation waters from the Paris Basin. *Chem. Geol.* 283, 226–241. doi:10.1016/j.chemgeo.2011.01.020

Négrel, Ph., Fouillac, C., and Brach, M. (1997). Occurrence of mineral water springs in the stream channel of the allier river (massif central, France): Chemical and Sr isotope constraints. *J. Hydrology* 203, 143–153. doi:10.1016/s0022-1694(97)00094-2

Okada, T., Matsuzawa, T., Umino, N., Yoshida, K., Hasegawa, A., Takahashi, H., et al. (2015). Hypocenter migration and crustal seismic velocity distribution observed for the inland earthquake swarms induced by the 2011 tohoku-oki earthquake in NE Japan: Implications for crustal fluid distribution and crustal permeability. *Geofluids* 15 (1-2), 293–309. doi:10.1111/gfl.12112

Onda, S., Sano, Y., Takahata, N., Kagoshima, T., Miyajima, T., Shibata, T., et al. (2018). Groundwater oxygen isotope anomaly before the M6.6 Tottori earthquake in Southwest Japan. *Sci. Rep.* 8 (1), 4800. doi:10.1038/s41598-018-23303-8

Palmer, M. R., and Edmond, J. M. (1992). Controls over the strontium isotope composition of river water. *Geochim. Cosmochim. Acta* 56, 2099–2111. doi:10.1016/0016-7037(92)90332-d

Pierotti, L., Botti, F., D'Intinosante, V., Facca, G., and Gherardi, F. (2015). Anomalous CO2 content in the gallicano thermo-mineral spring (serchio valley, Italy) before the 21 June 2013, alpi apuane earthquake (M = 5.2). *Phys. Chem. Earth Parts A/B/C* 85 (86), 131–140. doi:10.1016/j.pce.2015.02.007

Pierotti, L., Gherardi, F., Facca, G., Piccardi, L., and Moratti, G. (2017). Detecting CO 2 anomalies in a spring on Mt. Amiata volcano (Italy). *Phys. Chem. Earth Parts A/B/C* 98, 161–172. doi:10.1016/j.pce.2017.01.008

Reddy, D. V., Kumar, D., and Purnachandra Rao, N. (2017). Long-term hydrochemical earthquake precursor studies at the Koyna-Warna reservoir site in westernIndia. *J. Geol. Soc. India* 90 (6), 720–727. doi:10.1007/s12594-017-0781-x

Reddy, D. V., Nagabhushanam, P., and Sukhija, B. S. (2011). Earthquake (M 5.1) induced hydrogeochemical and δ18O changes: Validation of aquifer breaching-mixing model in koyna, India. *Geophys. J. Int.* 184 (1), 359–370. doi:10.1111/j.1365-246X.2010.04838.x

Rosen, M. R., Binda, G., Archer, C., Pozzi, A., Michetti, A. M., and Noble, P. J. (2018). Mechanisms of earthquake-induced chemical and fluid transport to carbonate groundwater springs after earthquakes. *Water Resour. Res.* 54 (8), 5225–5244. doi:10.1029/2017wr022097

Rozanski, K., Araguas-Araguas, L., and Gonfiantini, R. (1993). *Isotopic patterns in modern global precipitation*. Washington DC: American Geophysical Union Geophysical Monograph Series.

Schuessler, J. A., Kampf, H., Koch, U., and Alawi, M. (2016). Earthquake impact on iron isotope signatures recorded in mineral spring water. *J. Geophys. Res. Solid Earth* 121 (12), 8548–8568. doi:10.1002/2016jb013408

Scott, B. E., Newell, D. L., Jessup, M. J., Grambling, T. A., and Shaw, C. A. (2020). Structural controls on crustal fluid circulation and hot spring geochemistry above a flat-slab subduction zone, Peru. *Geochem. Geophys. Geosyst.* 21, e2020GC008919. doi:10.1029/2020GC008919

Snell, T., Paola, N. P., Hunen, J. V., Nielsen, S., and Collettini, C. (2020). Modelling fluid flow in complex natural fault zones: Implications for natural and human-induced earthquake nucleation. *Earth Planet. Sci. Lett.* 530, 115869. doi:10.1016/j.epsl.2019.115869

Sobolev, G. A. (1984). "The study of failure forerunners on the big samples," in *International symposium continental seismicity and earthquake precursors* (Beijing: Seismological Press), 515–524.

Su, Q., Yuan, D. Y., and Xie, H. (2016). Geomorphic Features of the Heihe river drainage basin in Western Qilian Shan-Hexi corridor and its tectonic implications. *Seismol. Geol.* 38 (3), 560–581. (in Chinese). doi:10.3969/j.issn.0253-4967.2016.03.005

Teufel, L. W. (1980). Precursive pore pressure changes associated with premonitory slip during stick-slip sliding. *Tectonophysics* 69, 189–199. doi:10.1016/0040-1951(80)90133-x

Thomas, D., Cuff, K., and Cox, M. (1986). The association between ground gas radon variations and geologic activity in Hawaii. *J. Geophys. Res.* 9I, 12186–12198. doi:10.1029/jb091ib12p12186

Tian, J., Pang, Z., Wang, Y., and Guo, Q. (2019). Fluid geochemistry of the Cuopu high temperature geothermal system in the eastern Himalayan syntaxis with implication on its Genesis. *Appl. Geochem.* 110, 104422–104442. doi:10.1016/j.apgeochem.2019.104422

Utkin, V. I., and Yurkov, A. K. (2010). Radon as a tracer of tectonic movements. *Russ. Geol. Geophys.* 51, 220–227. doi:10.1016/j.rgg.2009.12.022

Wakita, H. (1996). Geochemical challenge to earthquake prediction. *Proc. Natl. Acad. Sci. U. S. A.* 93, 3781–3786. doi:10.1073/pnas.93.9.3781

Wakita, H., Nakamura, Y., and Sano, Y. (1985). Groundwater radon variations reflecting changes in regional stress fields. *Earthq. Predict. Res.* 3, 545–557. doi:10.1007/978-94-017-2738-9_19

Wang, P., Song, X., Han, D., Zhang, Y., and Liu, X. (2010). A study of root water uptake of crops indicated by hydrogen and oxygen stable isotopes: A case in shanxi Province, China. *Agric. Water Manag.* 97, 475–482. doi:10.1016/j.agwat.2009.11.008

Wang, Y., Chen, J., and Chen, L. (2009). *Tracing groundwater with strontium isotopic compositions in the Hexi corridor basin, northwestern China*. Berlin/Heidelberg, Germany: Springer, 184–187.

Wang, Y., Li, Q., Ran, H., Zhao, C., and Liu, Y. (2018). Geothermal and seismic activities in the southeastern Tibetan plateau: Constraints from helium isotopes. *Bull. Mineral. Geochem* 37, 652–662. (in Chinese). doi:10.19658/j.issn.1007-2802.2018.37.103

Woith, H., Wang, R., Maiwald, U., Pekdeger, A., and Zschau, J. (2013). On the origin of geochemical anomalies in groundwaters induced by the Adana 1998 earthquake. *Chem. Geol.* 339, 177–186. doi:10.1016/j.chemgeo.2012.10.012

Wong, I., and Chapman, D. (1990). Deep intraplate earthquakes in the Western United States and their relationship to lithospheric temperatures. *Bull. Seismol. Soc. Am.* 80, 589–599. doi:10.1016/0040-1951(90)90455-H

Wu, G., Liu, J., Sun, Z., Li, J., Wang, C., and Zhou, Z. (2020). Hydrogeochemical characteristics of groundwater in jiuquan yumen-suzhou area of Hexi corridor. *Water Resour. Hydropower Eng.* 51 (10), 111–118. (In Chinese).

Xiong, L., Wang, J., and Pang, Z. (1990). Circulation depth of the thermal water in Zhangzhou geothermal field. *Sci. Geol. Sin.* 4, 377–384. (In Chinese).

Yang, H., Wang, D., Guo, R., Xie, M., Zang, Y., Wang, Y., et al. (2022). Rapid report of the 8 january 2022 MS 6.9 menyuan earthquake, Qinghai, China. *Earthq. Res. Adv.* 2 (1), 100113. doi:10.1016/j.eqrea.2022.100113

Yuan, D., Ge, W. P., Chen, Z. W., Li, C., Wang, Z., Zhang, H., et al. (2013). The growth of northeastern tibet and its relevance to large scale continental geodynamics: A review of recent studies. *Tectonics* 32, 1358–1370. doi:10.1002/tect.20081

Yuan, D., Zhang, P., Liu, B., Gan, W., Mao, F., Wang, Z., et al. (2004). Geometrical imagery and tectonic transformation of Late Quaternary active tectonics in Northeastern margin of Qinghai-Xizang Plateau. *Acta Geol. sin.* 78 (2), 270–276. (In Chinese).

Zhang, H., Zhang, P., Prush, V., Zheng, D., Zheng, W., Wang, W., et al. (2017). Tectonic geomorphology of the Qilian Shan in the northeastern Tibetan Plateau: Insights into the plateau formation processes. *Tectonophysics* 706-707, 103–115. doi:10.1016/j.tecto.2017.04.016

Zhang, P., Deng, Q., Zhang, G., Ma, J., and Gan, W. (2003). Active tectonic blocks and strong earthquakes in the continent of China. *Sci. China Ser. G.* 46, 528–624. doi:10.1360/02yw0305

Zhang, P., Zheng, D., Yin, G., Yuan, D., Zhang, G., and Li, C. (2006). Discussion on Late Cenozoic growth and rise of northeastern margin of the Tibetan Plateau. *Quat. Sci.* 26 (1), 5–13. (In Chinese).

Zhang, Y., Zhang, L., Chang, Y., Fan, Z., and Guo, D. (2018). Determining trace elements in rock samples containing refractory minerals by pressurize-microwave inductively coupled plasma mass spectrometry. *Uranium Geol.* 34, 105–111. (In Chinese).

Zhao, L. J., Eastoec, C. J., Liu, X. H., Wang, L., Wang, N., Xie, C., et al. (2018). Origin and residence time of groundwater based on stable and radioactive isotopes in the Heihe River Basin, northwestern China. *J. Hydrology Regional Stud.* 18, 31–49. doi:10.1016/j.ejrh.2018.05.002

Zoback, M. D., and Bverlee, J. D. (1975). The effect of micro-crack dilatancy on the permeability of westerly granite. *J. Geophys. Res.* 80, 752–755. doi:10.1029/jb080i005p00752

Zuza, A. V., and Cao, W. (2020). Seismogenic thickness of California: Implications for thermal structure and seismic hazard. *Tectonophysics* 782-783, 782228426–782228783. doi:10.1016/j.tecto.2020.228426